Nuclear Instruments and Methods in Physics Research A 847 (2017) 148–161

Contents lists available at ScienceDirect

Nuclear Instruments and Methods in Physics Research A

journal homepage: www.elsevier.com/locate/nima

The Tynode: A new vacuum electron multiplier

Harry van der Graaf[a,b,*], Hassan Akhtar[a], Neil Budko[a], Hong Wah Chan[a], Cornelis W. Hagen[a], Conny C.T. Hansson[a,b], Gert Nützel[d], Serge D. Pinto[d], Violeta Prodanović[a], Behrouz Raftari[a], Pasqualina M. Sarro[a], John Sinsheimer[c], John Smedley[c], Shuxia Tao[e], Anne M.M.G. Theulings[a,b], Kees Vuik[a]

[a] Delft University of Technology, Delft, The Netherlands
[b] Nikhef, Science Park 105, 1098 XG Amsterdam, The Netherlands
[c] Brookhaven National Laboratory, Upton, NY 11973, USA
[d] Photonis, Roden, The Netherlands
[e] Eindhoven University of Technology/DIFFER, The Netherlands

ARTICLE INFO

Keywords:
Photomultiplier
Dynode
Transmission dynode
Tynode
Trynode
Secondary electron yield
Pixel
Imaging
Surface termination
Cesiation
Work function
(Negative) Electron affinity
Planacon

ABSTRACT

By placing, in vacuum, a stack of transmission dynodes (tynodes) on top of a CMOS pixel chip, a single free electron detector could be made with outstanding performance in terms of spatial and time resolution. The essential object is the tynode: an ultra thin membrane, which emits, at the impact of an energetic electron on one side, a multiple of electrons at the other side. The electron yields of tynodes have been calculated by means of GEANT-4 Monte Carlo simulations, applying special low-energy extensions. The results are in line with another simulation based on a continuous charge-diffusion model.

By means of Micro Electro Mechanical System (MEMS) technology, tynodes and test samples have been realized. The secondary electron yield of several samples has been measured in three different setups. Finally, several possibilities to improve the yield are presented.

1. Introduction

The photomultiplier, in particular the electrostatic version developed after 1937, is still in use today because of its efficiency, time resolution and low noise. The latter is essentially due to its stack of dynodes, providing noise-free amplification-by-multiplication. In this work, the feasibility of a stack of micro dynodes is being explored. A new family of detectors for photons, electrons and energetic charged particles is proposed: a stacked set of curved miniature transmission dynodes called *tynodes* in vacuum, created through Micro Electro Mechanical Systems (MEMS) fabrication techniques on top of an all-digital CMOS pixel chip: see Fig. 1. This combination in itself is an efficient single free electron detector. By capping the system with a traditional photocathode, a highly sensitive single soft photon counter (Timed Photon Counter TiPC "Tipsy") can be realized. By capping it with an electron emission membrane 'e-brane', a Minimum Ionization Particle (MIP) tracking "Trixy" detector is realized with a time resolution far superior to current track detectors. Due to the double focusing effect above and below the domes, the device can work in magnetic fields (see Fig. 2). The tynode stack acts as an amplifier: this amplification-by-multiplication is essentially free of noise in terms of dark current, bias current and dark counting rate. The time resolution of this device can be in the order of a few ps since the electron crossing paths between two tynodes is two orders of magnitude smaller than in photomultipliers, and these paths are effectively uniform straight lines towards the next tynode, with little variation. The charge signal at the pixel input pad has a rise time of a few ps, determined by the crossing of the electrons of the gap between the last tynode and the pixel input

Abbreviations: ALD, atomic layer deposition; BSE, back scatter electrons; CBM, conduction band minimum; CMOS, complementary metal oxide semiconductor; DFC, Dual Faraday Cup; EA, electron affinity; FSE, forward scattered electrons; GEANT, Geometry and Tracking; MEMS, Micro Electronic Mechanical Systems; NEA, negative electron affinity; PE, primary electron; SEE, secondary electron emission; SEY, secondary electron yield; RSE, reflective secondary electrons; RSEY, reflective secondary electron yield; SEM, scanning electron microscope; TSE, transmission secondary electrons; TSEY, transmission secondary electron yield; UHV, ultra high vacuum

* Corresponding author at: Delft University of Technology, Delft, The Netherlands.
E-mail address: vdgraaf@nikhef.nl (H. van der Graaf).

http://dx.doi.org/10.1016/j.nima.2016.11.064
Received 25 June 2016; Received in revised form 25 November 2016; Accepted 29 November 2016
Available online 13 December 2016

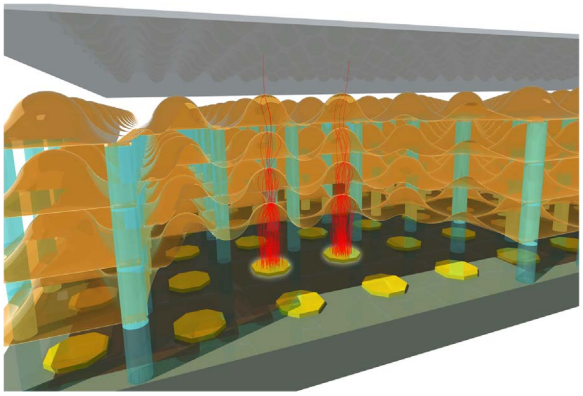

Fig. 1. The essence of the Tipsy detector: a stack of transmission dynodes in vacuum placed on top of a CMOS pixel chip. By capping the assembly with a classical photocathode, a photon detector "Tipsy" is realized. The Tipsy detector is sensitive for individual soft photons, which are converted into photoelectrons in the photocathode and multiplied in the stack of tynodes. The tynode's active dome sections focus the electrons onto the following tynode, yielding full acceptance. A number of $\delta_T{}^N$ electrons appears under the N-th tynode, assuming an average *transmission secondary electron yield* δ_T for each tynode. The resulting electron avalanche is detected by the digital circuitry in the individual pixels of the CMOS chip. The Timepix 1 and Timepix 3 chips [1] have shown to be well capable to process the incoming clouds of free electrons [2,3]. In a real Tipsy detector, the first tynode should be equipped with additional focusing electrodes, enhancing the acceptance of photo electrons. The last tynode should have sufficient shielding properties (conductivity) in order to realize the full development of the charge signal induced on the pixel input by electrostatic influention of the electrons crossing the last gap between the last tynode and the pixel chip [4].

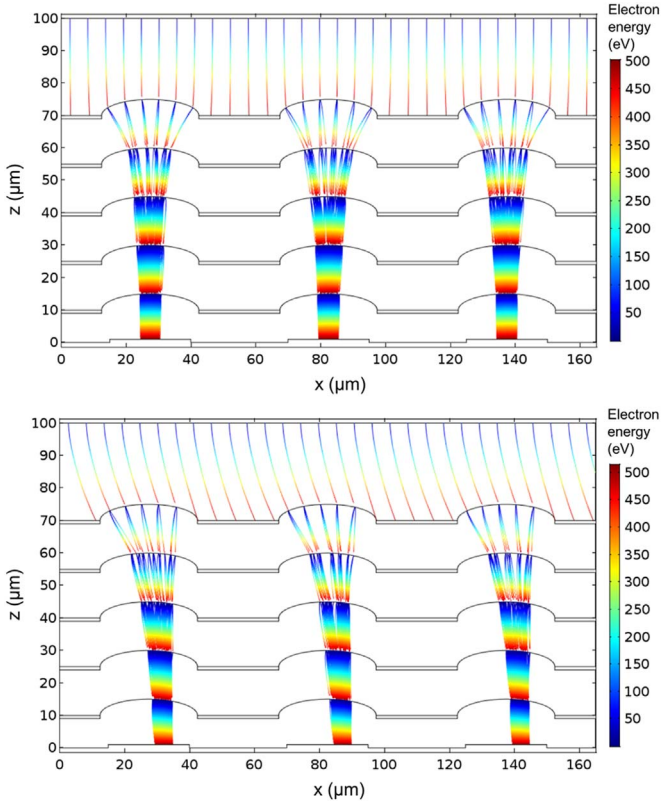

Fig. 2. Top: 2D simulated electron trajectories in Tipsy. The potential step between the electrodes is 500 V. Vertical spacing of tynodes: 15 μm, cone pitch is 55 μm (square). Incoming single electrons are generated in horizontal steps of 10 μm along the cathode. The color indicates the electron's energy in eV. Note the focusing effect of the dome shaped tynode structures. Bottom: the effect of a magnetic field of 1 T, demonstrating that the Tipsy photomultiplier could operate well in this magnetic field. (For interpretation of the references to color in this figure legend, the reader is referred to the web version of this article).

pad. The ultimate time resolution, however, may be influenced by a delay in the emission of secondary electrons after their creation in the tynode bulk material. Back-flow positive ions, created in the electron multiplication process, are blocked, so degradation of photocathodes or tynodes does not occur. Finally, these new planar detectors can be light, thin and flat, permitting, for instance, the hermetic readout of all six sides of a scintillating cube.

The core innovation, namely the stacked curved dynodes on top of a pixel chip, forming a light, compact and planar device, is also relevant for solid state, atomic and molecular physics experiments, for medical imaging (Cherenkov-PET [5]), and may have commercial applications such as prompt 3D optical imaging (machine viewing, driverless driving).

1.1. The Tynode

After the development of the photomultiplier, the advantages of planar transmission dynodes were recognised [6]. Although the creation of successful large-area film dynodes has been reported, the required primary electron energy was as high as a few keV, and the devices showed ageing effects. Since the secondary electron yield (SEY) of metals was known to be too low, insulators were applied and charge-up effects were observed in the relatively thick films. The conditions determining the transmission secondary electron yield (TSEY) are partly comparable to reflection secondary electron yield (RSEY) and can be described by three processes [7]: exciting, transport, and escape.

1.1.1. Exciting

Incoming primary electrons (PEs) transfer energy to electrons in the membrane, exciting electrons into the conduction band. The range of the primary electrons is determined by the primary electron energy and the membrane material.

In metals, the energy transfer is very efficient, though not desired, since all electrons in the conduction band participate: the minor energy increase of many electrons will vanish quickly by thermalisation, and very few electrons will escape. This explains, in general, the low SEY of metals. We define the **penetration depth** as the average distance between the PE impact point and the point where this electron comes to a halt.

1.1.2. Transport

In conducting materials, the energized secondary electrons will move through the membrane material, being quickly thermalized. In semiconductors and insulators, the lifetime of electrons and holes depends, among other things, on the scattering processes that can occur; wide band gap crystalline materials benefit from a dramatic reduction of electron-electron scattering for electrons near the conduction band minimum, significantly increasing their lifetime. This allows secondary electrons to travel a relatively large distance compared to conductors, where electron-electron scattering is predominant. The distance from the bulk to the surface, where secondary electrons are still able to escape is defined as the **escape depth**.

1.1.3. Escape

In conductors, few of the thermalised electrons will be able to cross the gap, due to the work function, escaping from the emitting surface into vacuum. In semiconductors and insulators, secondary electrons reaching the surface of the membrane can escape into vacuum if they possess enough energy to overcome the **electron affinity** (EA) of the emitting surface. Secondary electrons quickly thermalize to the conduction band minimum. In the presence of a positive electron affinity, the majority of the secondary electrons will be reflected/trapped. However, in case of a negative electron affinity (NEA), the secondary electron can be emitted into the vacuum freely.

High secondary electron emission (SEE) materials are often insulators. The emission of secondary electrons will inevitably leave

vacancies inside the membrane. The mobility of electrons and holes, and their diffusion therefore plays a role in SEE. The replenishing of vacancies is important to avoid charge-up effects.

Our goal is to develop a tynode with a high Transmission Secondary Electron Yield for incoming primary electrons with a low PE energy.

1.2. Transmission secondary electron yield (TSEY)

Most of the conditions mentioned above hold for reflective dynodes. An important condition for achieving a high-TSEY tynode is to have a low or negative electron affinity (NEA) at the emitting (here: bottom) side. For a tynode, the direction of the incoming primary electron is perpendicular to the tynode plane, where the angle of attack, in practice, in the case of reflection dynodes (and in MCPs) is much more slanted. The latter may result in a higher SE yield since most potential secondaries are created close to the emitting surface. The ratio of the reflective yield and the transmission yield depends on the escape depth, the penetration depth and membrane thickness. In addition, the interaction profile of potential secondaries along the path of the incident PE is of importance. The yields can only be calculated by performing detailed simulations based on models for low-energy interactions between an electron and matter.

In practice, ultra-thin films do not have free areas larger than a few mm^2, so the tynodes take the form of a rigid substrate, carrying an array of small-area membranes. For reasons of focusing these may have a dome shape. In addition, the dome geometry deals better with possible internal mechanical stress of the membranes.

Since more electrons leave a tynode than arrive, **charge-up effects** occur unless the (hole) conductivity of the material is sufficient. For a high-resistivity layer on a conducting carrier we can define its time constant $\tau=\varepsilon_r \cdot \rho$, where ε_r ($= k \cdot \varepsilon_0$) is the relative permittivity of the layer material, and ρ is its specific resistivity. In reality, a conductive thin coating can be applied on the top (PE landing) side of the membrane. After the emission of electrons at the bottom side, a positive surface charge, homogeneously distributed over the layer bottom surface, will 'vertically' leak away following an exponential decay with time constant τ, independent of the layer thickness. The time constant and the layer thickness define the local change in potential due to the deposit of positive charge with a certain density. This potential increase raises the electron affinity of the emitting surface, reducing the SEY. The hole mobility of an applicable membrane material is therefore of importance. A reflective dynode consists of a solid metal carrier, coated with a thin layer of high-RSEY material such as BeO, Al_2O_3, or MgO. Here, charge-up effects are limited since a conductor is never further away than the thickness of the layer. For tynodes this is different: here the nearest conductor may be at a distance equal to the radius of the active membrane area, which is several orders of magnitude larger than the membrane thickness. For having sufficient 'horizontal' conductivity, the membrane is coated on its impact side with a thin conductive layer that, at the same time, should absorb as little as possible of the energy of the incoming primary electron. Metals cannot be applied as conductive layer since this would cause incoming primary electrons to lose much of their energy, as mentioned above [7]. Still, some positive effects, associated with scattering, of using a thin Al or Au entrance layer on the TSEY have been reported [8]. We first applied sputtered C as conductive layer, but TiN is now preferred. Detailed simulations should lead to the best choice.

Another direct effect of vacancies is the reduction of SEY due to lower probability of an interaction with the incoming primary electron and the increased trapping of secondary electrons by the holes [9–11].

In Section 2, results of process analysis and (Monte Carlo) simulations are given. Section 3 sets out the processes and methods to fabricate prototype tynodes and special membrane test samples. Results of measurements of SEYs are given in Section 4, including comparison and discussion. In Section 5 roads leading towards a high TSEY are discussed.

2. Theory and simulations

Transmission secondary electron emission (TSEE) has the same principles as reflection secondary electron emission. There are, however, some distinctive parameters to consider. Density Functional Theory (DFT) is used to investigate the band structures of the material and the effect of surface termination: the electron affinity of membrane materials can be altered by implanting atoms onto the surface. A Monte-Carlo simulation: GEANT-4 is used to investigate the energy-loss distribution and electron-hole pair creation in tynode material. Finally, a charge transport model is used to study the charge-up behavior of insulators.

2.1. Negative electron affinity: density functional theory

The secondary electron yield depends largely on the electron affinity (EA) of the surface of the applied material. The EA of a semiconductor or insulator surface is typically calculated as the energy difference between the conduction band minimum (CBM) in bulk material and the vacuum level of the surface. If this level lies above the CBM, positive electron affinity is obtained; if it lies below the CBM, there is negative electron affinity (NEA), see Fig. 3. The NEA is one of the most favorable properties for electron emission materials. In a material with a negative electron affinity (NEA), any electron promoted into the conduction band will have enough energy to escape into vacuum. The EA can be altered by surface terminations, namely, adsorption of one single atomic layer atoms on the surface. A demonstration of the influence of the surface termination on the electron affinity is the large negative shift of electron affinity of the hydrogen terminated diamond compared to clean diamond surface, shown in Fig. 3. Using DFT calculations, a similar effect have been predicted for silicon nitride.

The application of NEA in the electron emission materials for photocathode technology has been extensively researched since 60's of last century. In 1958, Spicer [12] proposed the three-step model for photoemission and predicted the possibility of a NEA photocathode. The three steps proposed in this method are: excitation of the electrons in the bulk by photon absorption, electron transport to the surface of the material, and electron emission into vacuum. In 1965 the first NEA photocathode, using cesiated GaAs as the electron emission material was announced [13]. Here, cesium atoms are implanted onto the emitting surface, lowering the electron affinity by *surface termination*. Quantum efficiencies approaching 40% are now achieved using this new class of photocathodes. However, these cathodes have the well-known disadvantage of requiring UHV conditions after activation since the cesiated surface is easily contaminated due to its immediate reaction with oxygen when exposed to air.

Another important class of materials which exhibits NEA was Hydrogen-terminated diamond, which was initially described in 1979 by Himpsel et al. [14]. A literature survey of the last two decades reveals that diamond terminated with H, Cs or Cs-O has superb secondary electron emission properties [15]. One disadvantage of these surface terminations with NEA is that the surface species tend to desorb and the surface reconstruction occurs under ion and electron bombardment. Novel device configurations i.e. transmission dynode with NEA on the backside (as proposed in Tipsy), may overcome this problem since the fast electrons are slowed down after passing through the diamond films. One of the successful examples is the diamond-amplified cathode [16], where a diamond transmission dynode acts as an electron amplifier. The front side of the diamond dynode is coated with metal, while the back side is hydrogenated. The maximum secondary electron emission yield of 40 was measured in 500 μm diamond where the primary electrons had an energy of 10 keV. The hydrogenated diamond was demonstrated to be extremely robust with no degradation during the emission process, and with only a drop of

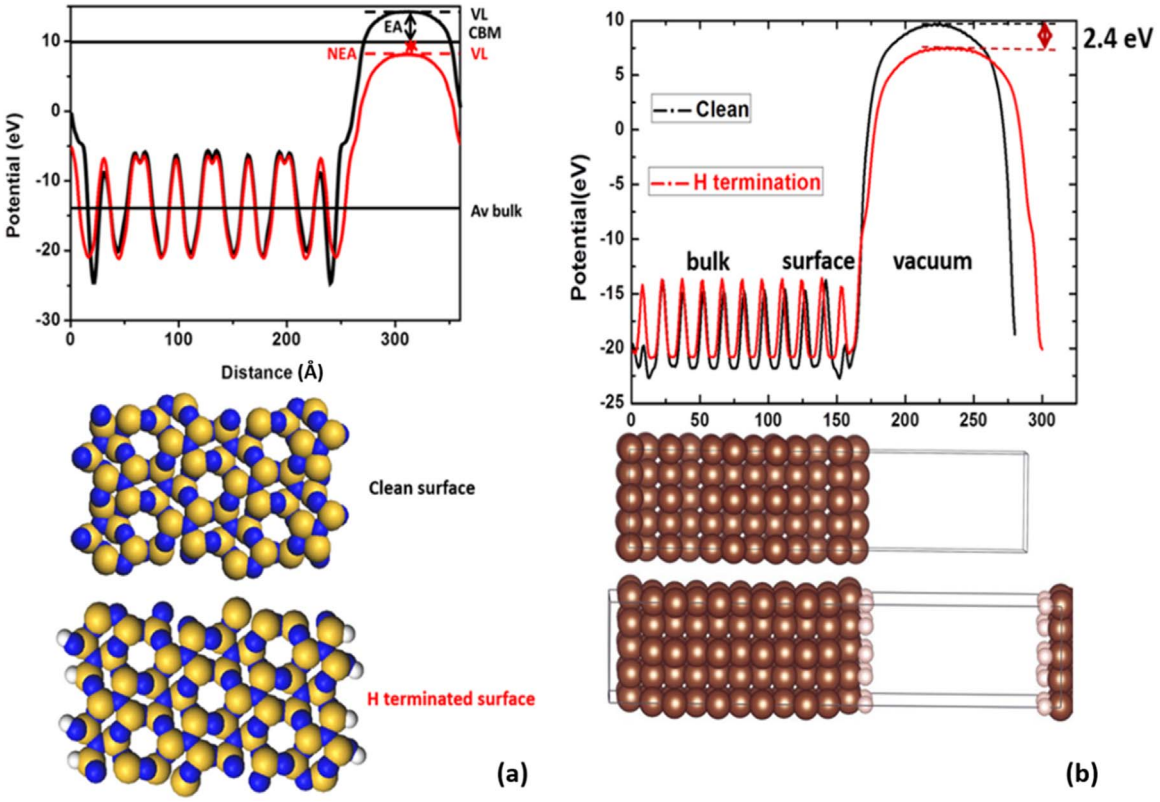

Fig. 3. Potentials across a clean and H-terminated β-Si_3N_4 (a) and diamond (b) slabs. Both potentials contains bulk, surface and vacuum regions. The potentials of the vacuum region are lowered by the one single atomic layer adsorption of hydrogen on the surface for both cases, resulting in a shift from positive electron affinity (EA) to negative electron affinity (NEA).

about 50% in electron emission gain after exposure to air for six months.

Inspired by applications of NEA materials summarized above, the feasibility of H, alkali metal, and alkali metal oxide terminations on ultra-thin silicon nitride dynodes has been explored by using Density Functional Theory (DFT) calculations [17,18]. For this, we applied the Vienna Ab-initio Simulation Package (VASP) [19,20]. Demonstrated in Fig. 3, H termination on silicon nitride (β-Si_3N_4) is predicted to have a similar effect to H termination on diamond, i.e. the possibility to induce NEA [11]. Alkali metal (oxide) terminations, generally induce even larger NEA (−2.1 to −4.4 eV) but with the compromise that they have lower bonding energies with silicon nitride and generally require UHV [18]. The general trend for alkali metal terminations on both clean and oxygenated surfaces is that the EA becomes more negative from Li to Cs, whereas the adsorption strength decreases from Li to Cs. In comparison, alkali terminations on oxygenated surfaces exhibit significantly higher stability than clean surfaces. Li termination on oxygenated surfaces is predicted to be the most promising candidate to induce NEA due to its high thermal stability and large NEA. The secondary electron emission measurements are shown in Section 4: the maximum RSEY of about 3.5 and TSEY of 2.5 have been obtained with an alumina (Al_2O_3) membrane. The effect of surface termination is expected to lower the EA and therefore to increase the SEY. These aspects are currently under study.

2.2. Monte Carlo method: low-energy extensions for GEANT-4

The transmission and reflection yields for alumina were calculated using a low-energy extension for GEANT4 [21], specially developed by Kieft and Bosch [22]. In this case alumina was chosen because the simulation results could be compared to experimental results of the reflection yield as well as the transmission yield. In the used Monte Carlo simulator, the emission of secondary electrons under irradiation of primary electrons is modelled by three different physical processes: elastic scattering, inelastic scattering and material-vacuum interface crossing. Elastic and inelastic scattering are governed by their respective cross sections. Here the models used are briefly discussed.

The elastic scattering cross sections at energies >100 eV were calculated using Mott cross sections [23]. For energies below 100 eV, the calculated Mott cross sections become very sensitive to the atomic potential used and the approximation breaks down. At energies <100 eV, the cross sections were calculated with the theory for elastic scattering of acoustic phonons as described in [22,24,25].

To model the inelastic scattering events Density Functional Theory (DFT) was used. In dielectric function theory the cross section for electron-atom interactions is derived from optical data. The total inverse mean free path is defined as:

$$\lambda^{-1}=\frac{1}{\pi E}\int \mathrm{d}\omega \int_{q_-}^{q_+}\frac{\mathrm{d}q}{q} Im[-1/\varepsilon(q,\omega)],$$

where ω is the total energy loss of the primary electron, q the momentum transfer from the primary electron to the secondary electron and $\varepsilon(q,\omega)$ the expanded dielectric function. Where q_+ and q_- follow from conservation of momentum of the primary and secondary electron to be:

$$q_{\pm}=\sqrt{2}(\sqrt{E}\pm\sqrt{E-\omega})$$

The dielectric function can be obtained from optical data $\varepsilon(0,\omega)$ by:

$$\mathrm{Im}[-1/\varepsilon(q,\omega)]=\frac{\omega'}{\omega}\mathrm{Im}[-1/\varepsilon(0,\omega')]$$

with the dispersion equation

$$\omega'=\omega-q^2/2.$$

where ω' is the zero-momentum energy transfer.

Electrons approaching the material-vacuum interface have to cross a potential barrier to escape the material. A quantum mechanical expression for transmission and reflection at a potential step was used

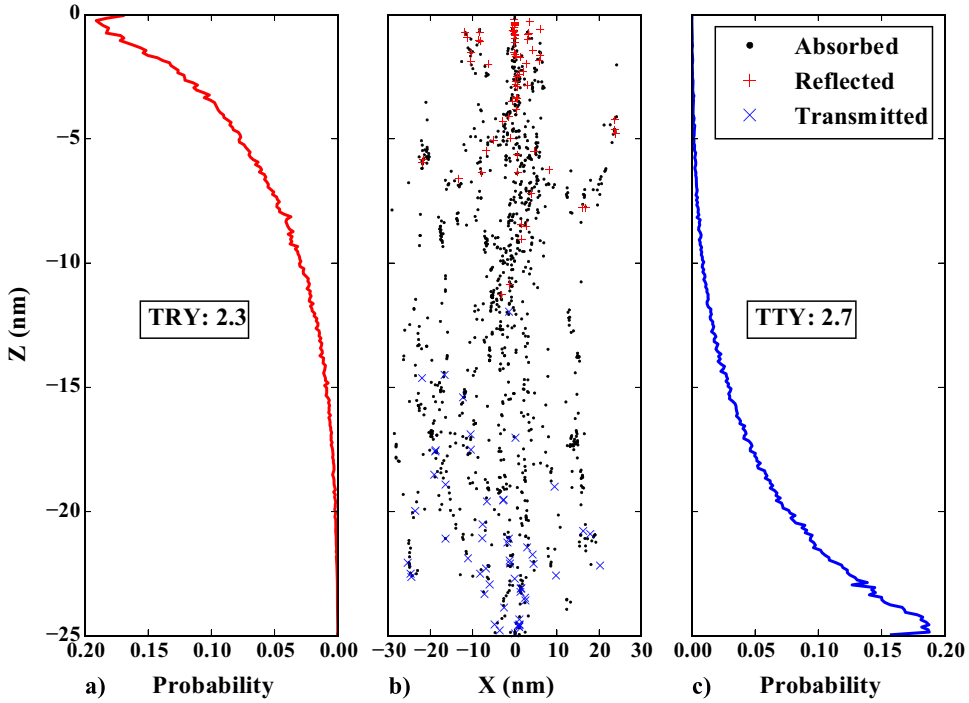

Fig. 4. Simulation of an alumina membrane (thickness 25 nm), bombarded with 2300 eV electrons. At this energy, the total transmission yield reaches its maximum of 2.7, and the total reflection yield at this energy is 2.3, although these absolute figures have no meaning. b) All points where electrons are created during a simulation with 30 PE's are shown. The + and x points denote creation points of electrons that were able to escape on the reflection respectively transmission side of the sample. The dots, which are plotted slightly smaller for clarity, denote creation points of absorbed electrons. *Z* is defined as the depth with respect to the irradiated surface. *X* is the distance to the beam position projected on the x-axis. a) The probability density function of the creation depth for electrons that leave the membrane on the top side. c) The same for electrons that leave the bottom side of the membrane.

to calculate whether the electron escapes the tynode or not [26].

In the simulations, alumina membranes with different thicknesses are bombarded with electrons from the top. Two electron detectors are simulated: the reflection detector is placed above and the transmission detector is placed below the sample. Some parameters in the simulation affect the escape depth of secondary electrons and the electron yield, such as the interaction cross sections, trap densities and electron affinity. The trap densities are not included in the model, since this is unknown for the alumina under investigation. In order to reproduce the reflection yield from the measurement on alumina in Section 4, the electron affinity of the alumina membranes was set to 9.3 eV. This is unlikely to be the real electron affinity, but altering this parameter will effectively reduce the escape depth as in the case where trap densities are included. The electron affinity is set to a value where the maximum yield corresponds to the measured data.

The positions where escaped and absorbed electrons were created in a 25 nm alumina membrane at 2300 eV are shown in Fig. 4. Electrons that are able to escape are mostly created in the 10 nm layer close to the escape surface. In Fig. 5, the same is displayed but with an angle of incidence of 45°.

The yield curves for a 10 nm and a 25 nm alumina membrane are shown in Figs. 6 and 7. The maximum of the total reflection yield for the 25 nm membrane is higher than that for the 10 nm membrane. This can be explained by the tail in the depth distribution of the creation points in Fig. 4. In the 10 nm membrane, this tail is simply cut off by the surface. The maximum of the total transmission yield is higher for the 10 nm membrane than for the 25 nm membrane, suggesting that the amount of secondary electrons created in the escape depth of the transmission side is less compared to the reflection side. For the reflection side, the maximum yield occurs where the range of the primary electrons are all within the escape depth. For transmission, energy is lost inside the membrane to electrons that cannot escape and only a small portion of the generated electrons are inside the escape depth. The primary energy at which the total transmission yield maximum occurs shifts to higher energies for thicker membranes because the primary electrons have to travel a longer distance through the membrane to reach the 10 nm bottom surface layer.

The maximum total transmission yield decreases even further when going from 25 nm membranes to 50 nm membranes, as shown in Fig. 8. Around 10 nm thickness, the total transmission yield reaches its maximum. Decreasing the membrane thickness below 10 nm results in the primary electrons shooting through the membrane without creating many secondary electrons, so the total transmission yield decreases for decreasing membrane thickness below 10 nm.

The energy distribution of transmitted and reflected electrons for a 10 nm alumina membrane at 1250 eV is shown in Fig. 9. Here it is clearly visible that at this energy, there is a small part of the primary electrons that pass through the membrane without losing energy.

Fig. 10 shows the distribution of the number of secondary electrons per event, both for transmission and reflection. Throughout this paper we refer to Secondary Electron Yield as the *average* number of emitted electrons after the impact of one primary electron. The output signal of a tynode stack follows from the n-fold convolution of the amplitude spectra of Fig. 10b. A low probability to have no transmission secondary electron at all is of importance only for the top tynode since this reduces effectively the efficiency of the (single electron sensitive) electron detector, and therefore the efficiency of, for instance, the Tipsy photon detector. This non-efficiency adds up to the non-efficiency of the photocathode. Other losses, for instance in the electron multiplication process, are not expected to occur due to the focussing effect of the domes in the tynodes.

2.3. Charge transport model

To acquire a better understanding of the charge transport in the dielectric membranes of the tynode on a larger time scale a recently developed self-consistent model [27] has been employed. This three-dimensional numerical model is based on the Drift-Diffusion-Reaction (DDR) system of equations augmented with a semi-empirical source function accounting for the ballistic transport stage. The advantage of

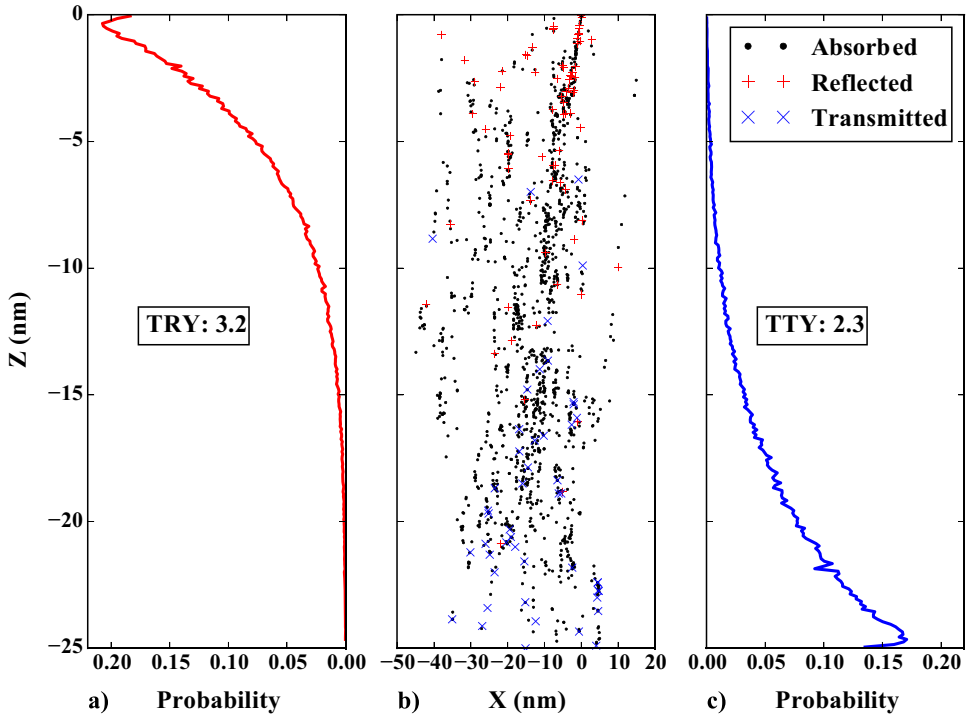

Fig. 5. As Fig. 4, but with angle of incidence of the PE's of 45°. The difference in TSEY and RSEY with respect to Fig. 4 reveals the essential difference between the two yields.

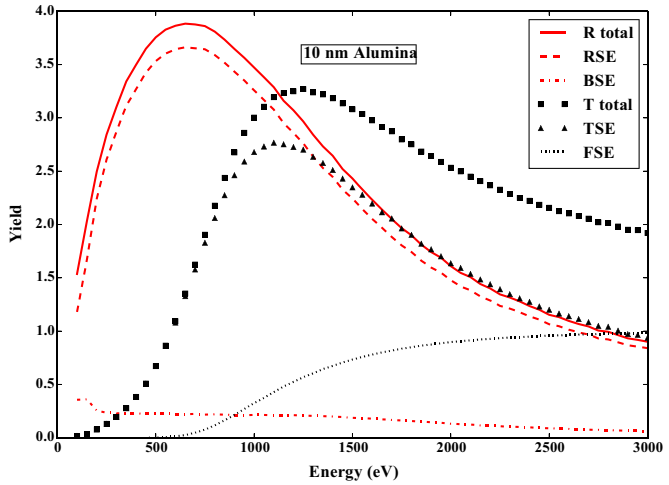

Fig. 6. The simulated yield curves for a 10 nm alumina membrane. The maximum total reflection yield (R total) is 3.9 and is reached at 650 eV. The maximum total transmission yield (T total) is 3.3 at 1250 eV. RSE is the reflection secondary electron yield, BSE is the back scatter yield. TSE is the transmission secondary electron yield, FSE is the forward scattered electron yield (the transmission equivalent of BSE).

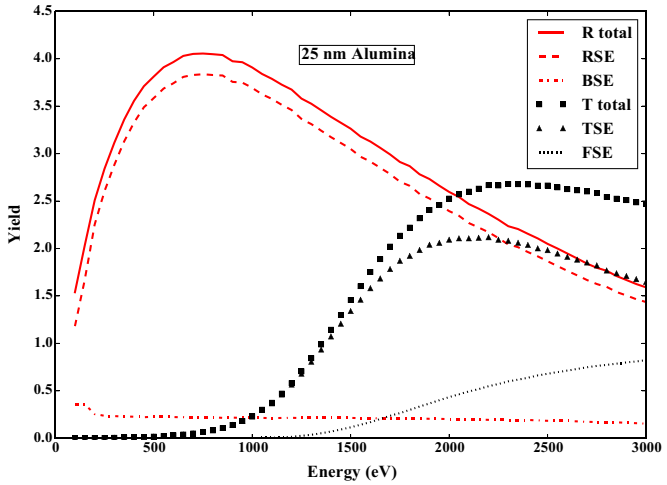

Fig. 7. The simulated yield curves for a 25 nm alumina membrane. The maximum total reflection yield is 4.1 and is reached at 750 eV. The maximum total transmission yield is 2.7 at 2300 eV.

this model is the possibility to study the trapping of electrons and holes and the sustained bombardment of the sample together with the associated charging phenomena. The gradual charging of electron-beam irradiated dielectrics causes the drop in the landing energy of Primary Electrons (PE) and the eventual reduction of the Secondary Electron (SE) yield to unity for all PE energies [28]. The latter effect has been observed both in DDR simulations and experimentally with the present alumina membranes and it was found that a TiN coating is instrumental in preventing it.

Although, the current uncertainty about the bulk properties of TiN does not allow for a very detailed model of the charge transport in this layer, one can assume that the TiN coating achieves a better electrical contact with the ground, providing a sink for the accumulated charge and/or a source of additional charges. Thus, in the present simulations we assume that the TiN layer simply provides an ohmic contact along its edge at the side of the alumina membrane. The membrane, including its TiN coating, is modelled presently as a uniform alumina disk of 300 nm radius with an ohmic contact along the upper 5 nm part of its edge. We consider two values for the thickness (height) of this disk: 20 nm and 30 nm.

Since most of the membrane measurements we performed with a focused SEM beam in the scanning mode, in our simulations we studied a sustained PE bombardment of the membrane surface for about 1 us at a typical SEM current value. The results are shown in Fig. 11, where the reflection, transmission, and total SE yield curves are given as functions of PE energy. The differences between this latter plot and the experimental results of Section 4 may be attributed to the simplified model of the TiN layer assumed in the simulations and uncertainties in our knowledge of the material parameters and SEM irradiation conditions.

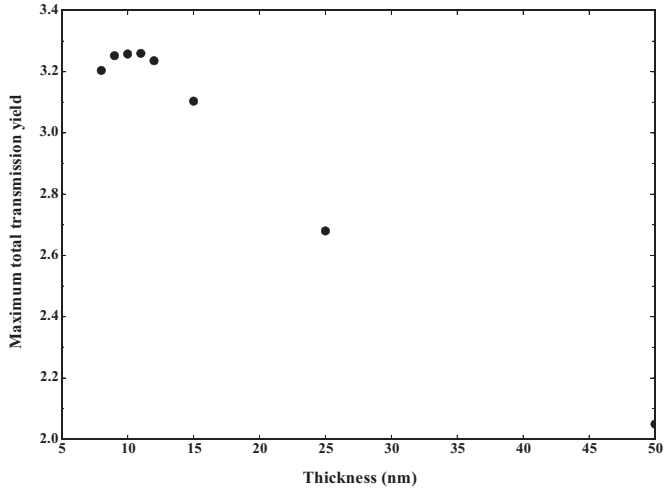

Fig. 8. The simulated maximum total transmission yield as function of membrane thickness for Alumina. The maximum total transmission yield is highest for thicknesses around 10 nm. If the thickness increases above 10 nm, the electrons created inside the membrane have a bigger probability to be absorbed before reaching the bottom surface. For thicknesses smaller than 10 nm, the primary electrons are likely to leave the membrane as forward scattered electrons before creating secondary electrons. Hence in both cases, the maximum total transmission yield decreases.

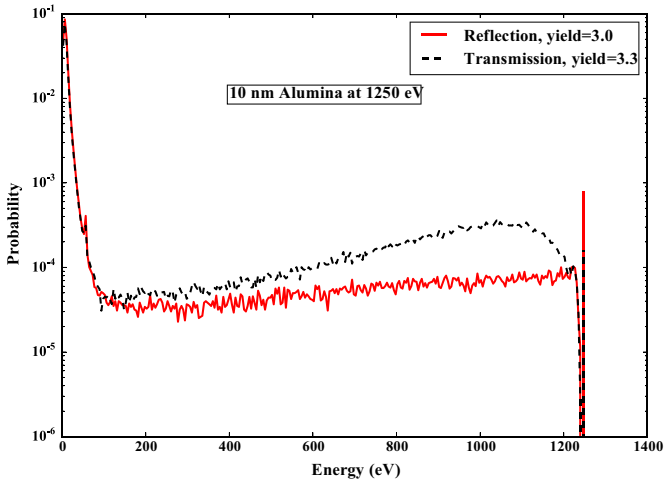

Fig. 9. The simulated energy distribution of electrons emitted by a 10 nm alumina membrane for the transmission (broken line) and reflection (solid line) side of the membrane. Vertical axis: probability per energy bin. The primary energy is 1250 eV. At this energy, the total transmission yield is 3.3, the total reflection yield is 3.0.

It is important to realize that the actual tynode membrane will not be operating under sustained focused bombardment, but rather with single PE's impacting the surface at more or less random time instants and random positions along the surface. The yield per single PE impact is known to be generally different from the yield under sustained bombardment. In fact, the yield from the very first impact is expected to be generally higher, since it is completely free from any charging effects. Subsequent impacts at the same spatial location along the membrane surface, however, will show different, possibly, lower yield values, unless the membrane is discharged in one or another way. Our simulations, where we consider the worst case scenario of sustained focused bombardment, show that providing an ohmic contact at the edge of the membrane helps to avoid these charging effects, since otherwise the total yield would have converged to unity for all PE energies. On the other hand, the effect of the TiN or any other (semi) conducting coating could be even more significant and needs further modelling and investigation. For instance, the bulk parameters of TiN (intrinsic charge density, mobility etc.) differ from those of the alumina, which may result in a junction layer at the TiN-alumina interface containing additional free electrons that may positively contribute to the transmission yield upon a single PE impact.

2.4. Material selection

Our simulations were focused on materials relevant for constructing tynodes. First, silicon nitride became available enabling the construction of ultra-thin and relative large areas with a certain conductivity, but with a rather low SEY. After that, ALD alumina became available, with the expected higher SEY. Recently we focus on ALD magnesium oxide, commonly used as dynode material in photomultipliers.

3. Fabrication

It is essential that the material of the tynodes is mechanically strong and exhibits high emission yield. For this application different materials were selected to enable the suspension of ultra-thin (10–50 nm) membranes with the required geometry.

3.1. Deposition of tynode materials

Layers are deposited by low-pressure chemical vapour deposition (LPCVD), a widely applied process in MEMS technology resulting in conformal layers with very good uniformity of thickness and composition [29,30]. LPCVD layers investigated here are silicon nitride (SiN) and silicon carbide (SiC). Depositions of SiN are performed in a hot-wall reactor with values of temperature and gas pressure set to 850 °C and 150 mTorr, respectively. Dichlorosilane (SiH_2Cl_2, DCS) is used as a source of silicon and ammonia (NH_3) as a source of nitrogen. Gas flow is varied in order to obtain a lower specific resistivity and investigate possible changes in stress. Here we investigated two SiN films with different silicon content: SiN_1 (Si/N=45/55) and SiN_2, richer with silicon (Si/N=50/50). Stoichiometry is measured via energy dispersive x-ray spectroscopy in a scanning electron microscope (SEM). Precursor gases employed for the growth of amorphous SiC layer at 760 °C are DCS and hydrogen acetylene (C_2H_2) diluted with hydrogen.

For alumina (Al_2O_3) and MgO films we applied atomic layer deposition (ALD) as a deposition method with very good control over thickness [31]. The synthesis of alumina from trimethylaluminium (TMA) and water is achieved in an ALD reactor at 300 °C, whereas MgO ALD was performed using sequential exposures of bis(ethylcyclopentadienyl) magnesium ($Mg(CpEt)_2$) and water at 250 °C.

3.2. Suspension of membranes

For investigation of SEY of mentioned materials, single free standing membranes 600–800 μm on a side are fabricated by MEMS techniques and cut into 1 cm×1 cm dies. As a substrate we use standard 4-in. single side polished < 100 > Si wafers, phosphorus-doped (5–10 Ω cm) and 525 ± 15 μm thick, covered with oxide as a stopping layer. Final release of membranes is achieved either wet (KOH) or via deep reactive ion etching (DRIE), depending on selectivity of materials. As examples, suspended SiN and alumina membranes are illustrated in Fig. 12. Fig. 13 shows an SEM image of a 25 nm thin alumina membrane.

For the production of 30–40 nm thin silicon membranes silicon-on-insulator (SOI) wafers are additionally oxidized and processed further. Other materials, such as different types of diamond and ALD AlN are currently under investigation as tynode candidates.

Additionally, we demonstrated the fabrication of an array of 25–40 nm thin SiN hemispherical membranes with diameters of 15–30 μm and 55 μm pitch. These membranes form a tynode suspended in a much thicker SiN layer, see Fig. 14. Curved geometry of protrusions is obtained by covering cylinders etched in silicon substrate by a material

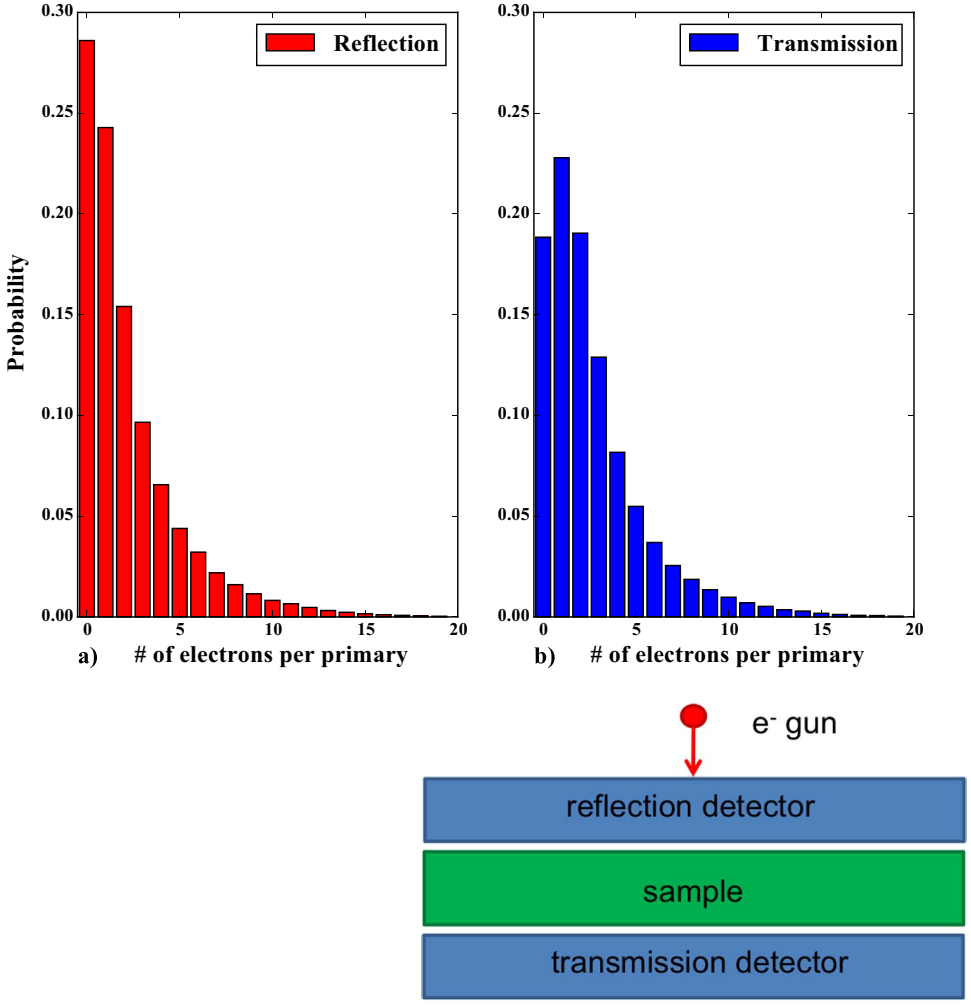

Fig. 10. Simulated distribution of number of electrons leaving the membrane per primary electron for a 25 nm Alumina membrane at a primary energy of 2300 eV (maximum transmission yield) in a) reflection and b) transmission mode. This yield is determined by averaging over many primaries, followed by normalisation.

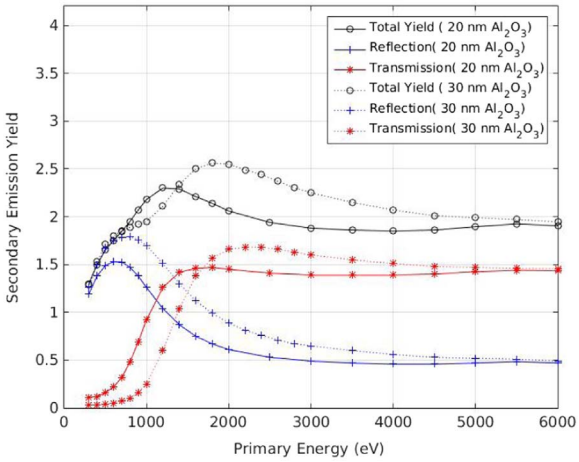

Fig. 11. Self-consistent simulation of reflection, transmission, and total secondary-electron yield from coated (edge-grounded) alumina membranes for two thickness values (20 nm and 30 nm) under sustained focused bombardment by primary electrons of different energies.

with a poor step coverage. The space around membranes is coated with a conductor (gold) which replenishes electrons extracted from membranes and serves as a contact for measurements of secondary electron emission. A conductive layer can be applied as a heater that facilitates bake-out cleaning at elevated temperatures.

Fig. 12. Schematic (not to scale) drawing of suspended alumina (up) and SiN (below) single membranes fabricated for measurement of SEY.

Such pixilated tynodes, containing an array of dome-shaped membranes, could be subsequently stacked to form a hybrid electron multiplying unit. TiPC can greatly benefit from ALD processes which can be performed even at temperatures below 100 °C, allowing at the same time the use of polymers in a support template between tynode stacks [32].

4. Results of measurements

The secondary electron yield of material samples and prototype tynodes has been measured with the following setups:

1. **The SEM/Dual Faraday Cup setup**. The RSEY can be measured

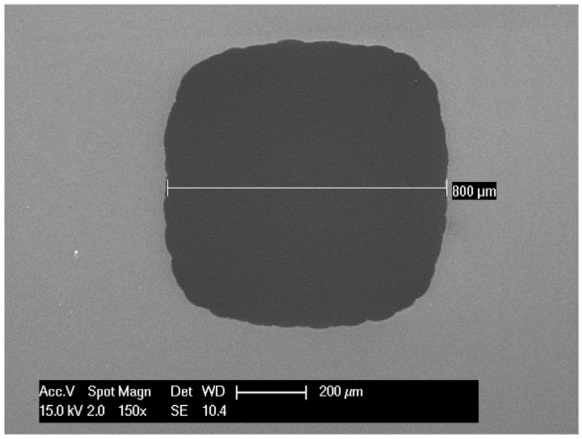

Fig. 13. SEM image of suspended 25 nm thin alumina membrane. This ALD layer looks smooth and no surface irregularity such as wrinkling due to a high stress is observed.

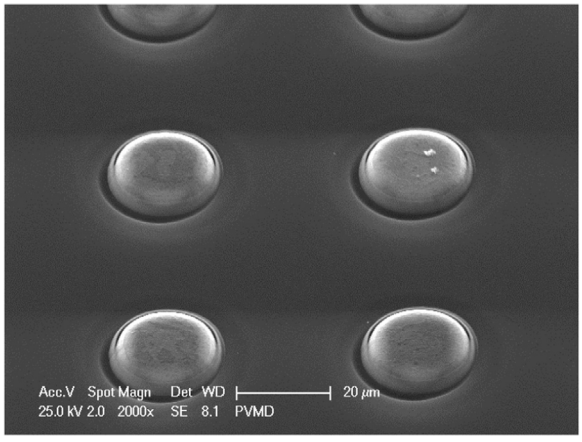

Fig. 14. SEM image of a section of 64×64 dome-shaped 25 nm thin SiN membranes forming a pixelized tynode. Capture is taken before final backside etching.

directly in the SEM, and by placing the sample into a multi-electrode cavity, all current components can be obtained separately. The imaging power of this setup is of great importance, but the vacuum cannot be better than 10^{-6} mbar, so surface contamination may prohibit testing samples with critical surface sensitivity.

2. **DyTest Brookhaven.** Primary electrons from an e-gun are directed onto a sample. By varying the potential of the sample, the RSEY can be obtained.
3. **Fowler measurement**. Here the sample is irradiated with a monochromatic light beam with constant intensity and variable wavelength. The emitted photo-current as a function of the wavelength reveals the electron affinity of the sample surface.
4. **Photonis, Roden, The Netherlands.** This concerns a general-purpose setup for measuring SEY, including an e-gun, multi-sample holders and a variety of electron detectors. This UHV system includes cleaning and bake-out facilities.

4.1. The SEM/Dual Faraday Cup setup

This a special setup built for transmission secondary electron measurements inside a scanning electron microscope (SEM). For this, the Dual Faraday Cup (DFC) setup is mounted on the sample stage inside the SEM (FEI NovaNanoLab 650 Dual Beam). Transmission measurement require a more precise electron beam compared to reflection measurements due to the size of the tynodes, which have a surface area of less than a mm^2. The imaging capabilities of the SEM are used to locate the tynode and to ensure that only the 'active' (ultra-thin) part of the tynode is being irradiated. The Dual Faraday Cup

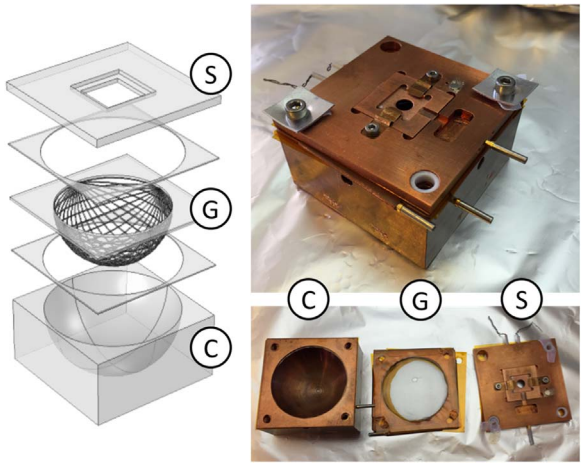

Fig. 15. The Dual Faraday Cup (DFC) setup consisting of three electrodes: the sample holder (S), retarding grid (G) and collector (C). The electrodes are electrically insulated by Kapton foils and can be biased.

setup consists of a copper sample holder, a retarding grid and a copper collector, see Fig. 15. Each electrode is isolated from each other and connected via a feedthrough to a Keithley 2450 Sourcemeter. Each electrode can be biased from −200 V to +200 V, while the currents are measured simultaneously. The SEM has an electron source that can be operated with 0.3–30 keV electrons with a beam current of a few pA to a few nA. The beam current is measured with a small Faraday Cup inside the sample holder. For the measurement of transmission yields, we only applied the lower section of the DFC. The vacuum is between 10^{-5} and 10^{-6} mbar.

The rate at which electrons are deposited on the surface plays an important role in the charge-up behavior of an insulator. To keep the dose rate small, and therefore the charge-up, either the beam current can be decreased or the scan area can be enlarged. The degree to which the sample charges is determined by the time in which the dose is delivered to the sample, i.e. the dose rate eq. (1). When the electron beam with beam current I_B is scanned over a surface area A_{frame} during a total exposure time t, the average dose $< D >$ is given by

$$\langle D\rangle = \frac{I_B \cdot t}{A_{frame}}$$

where I_B the current in nA and A_{frame} the surface of the frame in m^2.

The average electron dose rate is given by

$$\frac{d\langle D\rangle}{dt} = \frac{I_B}{A_{frame}}$$

given in $C/(s\,m^2)$. To keep the dose rate small, and therefore the charge-up, either the beam current can be decreased or the scan area can be enlarged.

The DFC method is a sample-biasing method in which two separate measurements are done [33]. The electron yield depends on the electron energy E of the primary electrons. In the first measurement the sample is negatively biased (−50 V). The total transmission electron coefficient σ_T is measured directly and is given by

$$\sigma_T(E) = \frac{I_{RG,-} + I_{C,-}}{I_B}$$

with I_B the electron beam current, $I_{RG,-}$ the retarding grid current and $I_{C,-}$ the collector current measured with a negatively biased sample. The total reflection electron coefficient σ_R is measured indirectly and is given by

$$\sigma_R(E) = \frac{I_B - I_{S,-} - I_{RG,-} - I_{C,-}}{I_B}$$

with in addition $I_{S,-}$ the sample current measured with a negatively

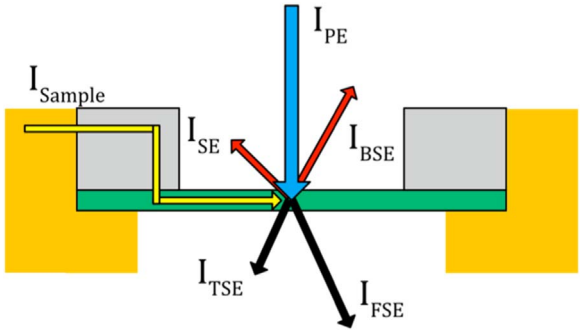

Fig. 16. The currents to and from a sample irradiated with a beam of (primary) electrons.

biased sample: see Fig. 16. The total reflection and transmission coefficient does not distinguish true secondary electrons from the higher energetic backscattered electrons (BSE) and forward scattered electrons (FSE). A second measurement with a positively biased sample is needed to separate them. A positively biased sample (+50 V) allows BSE (> 50 eV) and FSE (> 50 eV) to be collected by the collectors, while secondary electrons (< 50 eV) are recaptured. The forward scattered electron coefficient $\tau(E)$ is given by

$$\tau(E) = \frac{I_{RG,+} + I_{C,+}}{I_{beam}}$$

with $I_{RG,+}$ the retarding grid current and $I_{C,+}$ the collector current for a positively biased sample. The backscattered electron coefficient η is given by

$$\eta(E) = \frac{I_{beam} - I_{S,+} - I_{RG,+} - I_{C,+}}{I_{beam}}$$

with in addition $I_{S,+}$ the sample current measured with a positively biased sample. The reflective secondary electron coefficient δ_R is then given by

$$\delta_R(E) = \sigma_R(E) - \eta(E)$$

and the transmission secondary electron coefficient δ_T by

$$\delta_T(E) = \sigma_T(E) - \tau(E)$$

The reflection electron coefficient of various common MEMS/IC technology materials is measured with the DFC setup. The thin films are deposited on a p-type silicon substrate. Conductive silver paint is applied to the sides of the samples to improve the electrical contact between the silicon substrate and the copper sample holder. The samples are measured as-received without bake-out. The results are shown in Fig. 17 and Table 1. Also, they are in agreement with the literature considering that the samples are measured as-received (Table 1). Surface cleaning by heating and/or sputtering has been shown to increase the electron yield, as in the case of MgO, or decrease, as in the case of Al_3O_4 [33]. The thickness of the thin films also plays a role in the obtained reflection yield [34].

The transmission electron emission coefficients of a tynode have been measured: see Figs. 18 and 19. The tynode consists of a high SEE layer of aluminium oxide with a thickness of 25 nm and a conductive layer of titanium nitride with a thickness of approximately 5 nm on top. The black curves are the reflection yields from the conductive titanium nitride. The red curves are the transmission yields from the SEE layer of aluminium oxide.

One fundamental limitation of the SEM measurements is the best possible vacuum of order 10^{-6} mbar. In such an environment, the formation of surface contamination is not excluded: even after a bake-out, water and hydrocarbon molecules will quickly be attached, influencing the electron affinity of the surface. The effect of surface contamination (and surface termination) has to be performed in an ultra-high vacuum (UHV) setup. Therefore, the reflection yield of some

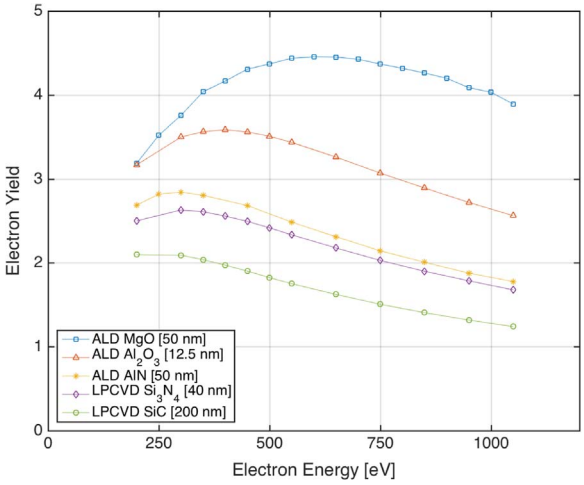

Fig. 17. Total reflection electron yield of MEMS/IC materials.

samples has been measured in different setups with UHV, including an industrial standard setup, to compare the yields. The reflective yields do not differ a lot, but contamination does affect the yield.

Finally, in Fig. 19 the transmission yields of ALD alumina tynodes with a TiN conductive coating are shown. The measured maxima of the TSEYs are in good agreement with the simulations shown in Figs. 6 and 8, albeit that the electron affinity assumed in the simulation has been adapted to match the absolute values of the measured RSEY and TSEY. The measured position of the optimal yields, in terms of PE energy and membrane thickness, is in very good agreement with both the low-energy GEANT-4 simulations and the results of the Charge Transport model (Fig. 11 right). We conclude that the transmission secondary electron yield of a thin homogeneous Al_2O_3 membrane reaches a maximum of 2.5 for a thickness of 10 nm, for an energy of the incoming primary electrons of 1200 eV. The transmission secondary electron yield, under these conditions, is 20% lower than the reflective secondary electron yield.

4.2. DyTest Brookhaven

Samples are mounted to an electrically isolated aluminium holder and connected to a Keithley 6517A electrometer to bias the holder and measure current. Secondary electron yield is measured using a Kimball Physics ELG-2 electron gun. The incident electron beam current is measured by positioning the electron beam on the sample holder, put at a positive bias potential, for a given electron gun energy. Reflective secondary electron current is measured with a negative bias to repel any secondary electrons escaping the sample. Reflective secondary electron yield is calculated as the difference between primary current and secondary electron current divided by the primary current, with both currents measured at each energy setting. The energy values are corrected to correspond to the energy of electrons landing at the sample surface, accounting for the sample bias. Measurements were performed using a low electron gun current of 0.3 μA and a circular spot size of 10 mm in vacuum of less than 10^{-8} mbar. In this low current density regime, sample charging effects were only seen on the 150 nm SiC thin film sample with higher electron energies. A large enhancement of the reflected secondary electron yield was observed for the Al_2O_3 coated SiN thin film sample: see Fig. 20.

With these measurements we have confirmed documented RSEY values of several materials. The UHV environment and bake-out and other cleaning facilities allow us to perform studies on surface termination with cesium, hydrogen, or boron.

Table 1
Summary of reflective SEY measurements.

Material	DFC/SEM setup			Brookhaven DYtest		Literature			Ref.
	Film thickness (nm)	E_{max} (eV)	δ_{max}	E_{max} (eV)	δ_{max}	Film thickness (nm)	E_{max} (eV)	δ_{max}	
Si	40	~250	~1.2	–	–	N/A	~300	~1.2	[52]
LPCVD Si_3N_4	40	300	2.6	300	2.4	10	~350	~2.9	[38]
LPCVD SiC	200	~250	2.1	250	2.1				
ALD Al_2O_3	12.5	400	3.6	400	3.5	20	~380	~3.7	[33]
ALD MgO	50	600	4.4	–	–	20	~800	~5.2	[33]

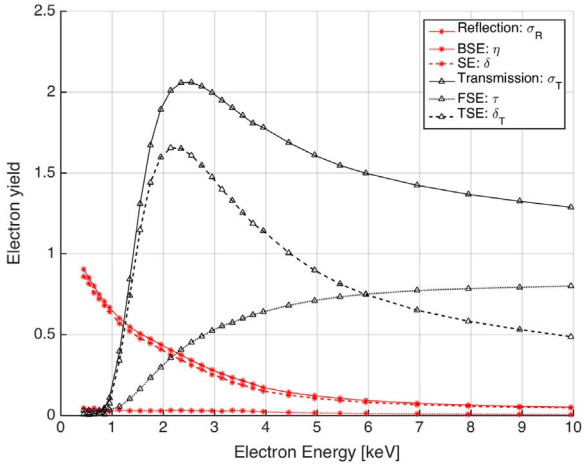

Fig. 18. Electron emission coefficients of a Tynode consisting of a conductive titanium nitride layer (5 nm) and a high SEE layer of ALD aluminium oxide (25 nm). (For interpretation of the references to color in this figure legend, the reader is referred to the web version of this article).

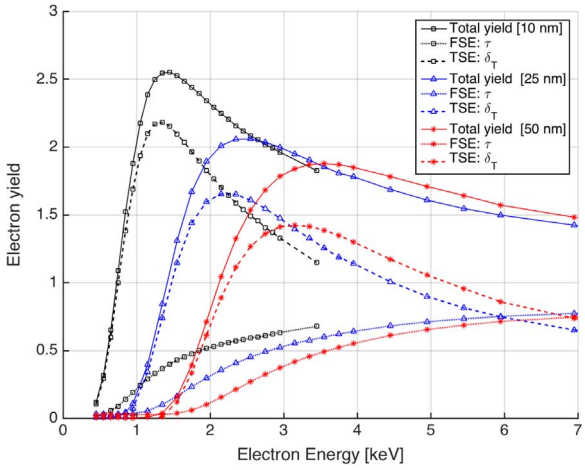

Fig. 19. Transmission electron emission coefficients of a Tynode consisting of a conductive titanium nitride layer (5 nm) and a high SEE layer of ALD aluminium oxide (of 10, 15 and 25 nm). The three TSE curves, associated with 'punch through' electrons, approach the value of 0.8 for high energy primary electrons. The correct value is 1: this is a known instrumental effect related to a non-perfect radial electric field in the Dual Faraday Cup. (For interpretation of the references to color in this figure legend, the reader is referred to the web version of this article).

4.3. Fowler measurement

Information about the electron affinity of a surface can be obtained by registering the photocurrent induced by irradiating the surface with soft photons with variable energy (thus wavelength). Photoemission measurements were used to determine the work function of samples using Fowler's law [35] and demonstrate reduction of the work function and electron affinity by cesium surface layer termination.

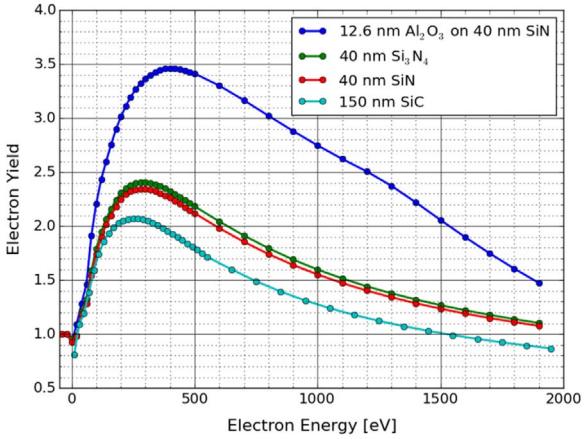

Fig. 20. The reflective secondary electron yield of four different samples.

The increase of photoelectrons escaping into the vacuum at energies above the work function is related to the ranges of escape angles available. For most metals, the increase in the square root of quantum efficiency is proportional to the increase in photon energy above the work function [36]. Samples were heated to 550 °C to clean the surfaces prior to measuring photoemission. A custom built monochromatic light source was used to induce photoemission, and a biased anode close to the sample collected the photocurrent. Using this system, the work function of aluminium was measured as 4.05 ± 0.05 eV, consistent with previously measured values [37]. Photoemission of a 40 nm thin film of Si_3N_4 is shown in Fig. 21. A linear fit of the square root of the quantum efficiency near the photoemission threshold yields a work function of 3.30 ± 0.04 eV. Note that as the SiN is a defect-rich amorphous film, this energy likely represents the energy spacing between the Fermi level and the vacuum

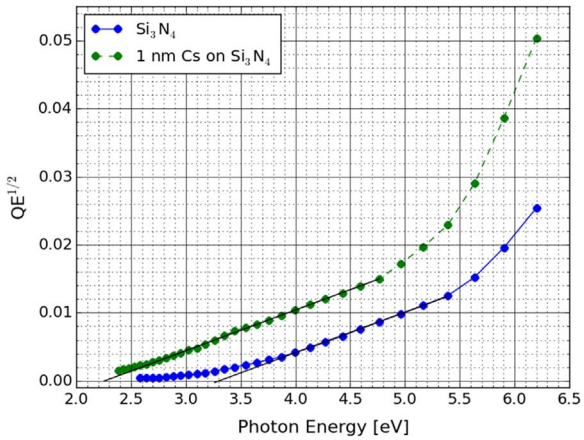

Fig. 21. A Fowler plot of a Si_3N_4 sample, before and after cesium termination, with a linear fit to the square root of the quantum efficiency, near the work function. The extrapolated x-intercept of the linear fit is the energy needed to remove an electron from the surface, showing a considerable reduction from cesiation.

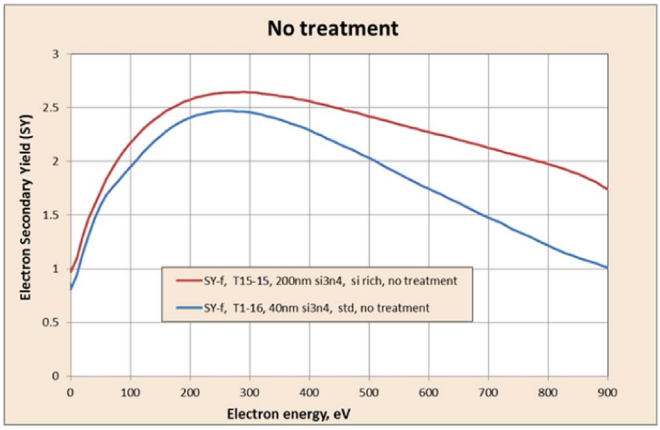

Fig. 22. The reflective secondary electron yield as a function of the energy of the incoming electron, for a SiN sample, before possible treatments such as cesiation.

(as there are likely excitable defect states just below the Fermi level in the SiN). After deposition of a 1 nm cesium surface layer, the work function decreases to 2.26 ± 0.04 eV. Secondary electron yield should also improve with cesium surface termination: this measurement is underway.

4.4. Photonis, Roden, The Netherlands

In a dedicated setup, with a vacuum level better than 10^{-10} mbar, the RSEY was measured of SiN samples, confirming earlier results [38]. Also, the expected higher RSEY of SiN samples covered with ALD alumina has been observed. The setup has excellent bake-out and surface cleaning facilities and measures the absolute SEY's with high precision: see Fig. 22.

4.5. Precision of the measurements

The yields presented in this chapter are ratio's of currents or differential currents. The noise is the measured currents results in relatively small uncertainties: data points follow closely a SEY curve with its typical maximum, indicating the low noise in the currents. The absolute SEY value, however, may very due to charge-up effects, surface contamination and surface modification. The precision of SEY measurements can only be estimated after combining many measurements under different conditions, using a set of samples. We estimate the error is the SEY measurements to be 10% for the SEM and Brookhaven data, and 5% for the data from Photonis, thanks to the permanent dedicated set up.

Comparing results from simulations and measurements we conclude:

1. The optimal TSEY is reached if the membrane thickness corresponds to the escape depth of secondary electrons.
2. The highest reflection yield is always higher than the highest transmission yield, as the generation of electron-hole pairs on the impact side is always more favorable.
3. Since most secondary electrons originate from close to their emission surface, the optimal PE energy is much higher for transmission electron emission with respect to reflection electron emission; the difference is related to the energy loss profile of perpendicular incident PEs in the membrane.

5. Outlook

With state-of-the-art MEMS technology it seems possible to construct tynodes in the form of a carrier with an array of dome-shaped membranes. Assuming that focusing prevents acceptance losses, a stack of 6 of the best tynodes mentioned above results in a gain of 250, enough to drive the circuitry in the pixels of a TimePix chip [1]. We will continue to improve the tynode: a higher TSEY at lower primary electron energy would reduce the complexity of fabricating the tynode stack. As a membrane material, MgO is reported to have a significantly higher RSEY than alumina [39,40]. There are also many reports about a very high RSEY of diamond, although there is much spread in measured data: yields vary with the type of diamond, its crystal orientation, and surface conditions [41]. For a single-crystal diamond, a yield of 84 has been reported. The crystallinity of the diamond film plays an important role in the transport of secondary electrons [33]. At present, the limiting factor to use diamond as a tynode is the fabrication of ultra-thin high quality diamond films. Another candidate material is GaAs [42].

Proper surface termination reduces the electron affinity and can even result in a Negative Electron Affinity (NEA). Hydrogen termination has been shown to increase the RSEY of diamond, and is expected to work in a similar way for SiN (Section 3). Applying Cesium onto the emitting surface has been shown to favour the RSEY, but the cesiation of materials may be impractical in view of an immediate reaction when exposed to air (see Fig. 21).

The accelerating field, required for the energy increase of electrons on their way to a next tynode, has an intrinsic positive extracting effect on the TSEY. There is a region in which this electric field causes an increase of the yield before "cold" field emission occurs: this is described as sub-threshold emission [43]. Not only is the electron work function reduced (due to the Schottky effect): the field may propagate into the bulk of the membrane if this is an insulator, covered by a conducting layer at the impact side. If the hole mobility is sufficient, the material could be an insulator without suffering charge-up effects. With such a field assisted tynode, electrons in the conduction band will drift towards the emitting surface, increasing the TSEY. One of the first transmission dynodes, made of low density/porous materials, has been reported to have a TSEY of 8.4 [8]. The SEE mechanism of such materials is different in nature compared to dense crystalline material. As a result of charging inside the porous material, strong electric fields appear inside the cavities of the material. Secondary electrons that are generated inside the material will cause a new cascade of electrons [44]. Such an active tynode "trynode" could take the form of a film, sandwiched by two conducting layers put at different potential. There are reports on the use of MgO-covered carbon nanotubes as a SEE material. The SEE mechanism is comparable to that of porous materials. The sharp tips of the covered carbon nanotubes will cause strong electric fields near the tips: gain of 10^3 has been reported [45].

Metals are not well suited to be used as the conductive layer at the impact side of a tynode since, for instance, a 1 keV electron loses practically all of its energy passing through a layer of 2 nm thick Au. Graphene is another candidate for a conductive material. We will perform a dedicated study using Monte Carlo (Geant4) simulations to select the best (hole) conducting material.

With a TSEY of 4, a stack of 4 tynodes results in charge pulses of 256 electrons, enough to drive the pixel circuitry of the TimePix-3 chip. By manually stacking these tynodes onto the pixel chip, a hybrid Tipsy prototype can be made. A stack of 8 of these tynodes would create 65 k electrons, enough to drive the circuitry of an all-digital CMOS pixel chip, omitting an amplifier per pixel. After that, MEMS wafer post processing could be developed to create monolithic detectors. In parallel, the search for higher TSEY at lower primary energy should continue, reducing the required number of tynodes.

5.1. High QE photocathodes

Photocathodes are typically used to convert photons to electrons in single soft photon sensitive devices, especially those which rely on vacuum multiplication for gain (Tipsy, photomultipliers, LAPPD [46],

Planacon [47]). A large effort has gone into development of methods for large-area growth of soft photon sensitive cathode materials [48,49], with the goal of achieving efficient photocathodes quickly and cheaply. The geometry of Tipsy puts additional requirements on the photocathode – the need to achieve electron energies similar to those used in a PMT but with two orders of magnitude more compact geometry necessarily leads to higher electric fields, fields more similar to those found in accelerator cavities. This in turn requires that the surface morphology of the cathode be considered – traditional photocathode growth methods produce cathodes which can be very rough (25 nm RMS roughness for a 50 nm thick film [50]). Recent progress on accelerator photocathodes, including direct sputtering of the alkali antimonides [51], has resulted in a marked reduction in the film roughness, with sub nm roughness now achievable. It is expected that such growth techniques will achieve a photocathode with sufficiently small dark field emission rate for Tipsy to function.

These growth techniques may, together with newly acquired theoretical knowledge, enable the development of a new generation of photocathodes with a QE well above 0.5.

6. Conclusions

The transmission secondary electron yield of a thin homogeneous Al_2O_3 membrane reaches a maximum of 2.5 for a thickness of 10 nm and an energy of the incoming primary electrons of 1200 eV. The reflective secondary electron yield, under these conditions, is 20% higher. The yields are strongly determined by the electron affinity of the emission surface, and by the escape depth of secondary electrons. The required energy of the incoming primary electrons is very high when compared to the corresponding case of the dynodes in photomultipliers (100–200 eV). The measured values are in good agreement with the results from simulations and theoretical analysis, albeit that some simulations do not (yet) predict the absolute value of the yields. The SEM measurements clearly showed charge-up effects (not presented in this paper). The (hole) conductivity of the membrane, and the 'horizontal' conductivity should be sufficient to replenish vacancies in order to limit charge-up effects. This is possible by a 3 nm thick layer of TiN, albeit that the local energy loss of incoming primary electrons is considerable.

With a stack of tynodes mentioned above, a practical vacuum electron multiplier could be made: placed on top of a Timepix-3 pixel chip, a new generic digital single electron detector is within reach. There are several possibilities, however, to increase the tynode transmission secondary electron yield, and to reduce the required landing energy of the incident primary electrons. This would significantly reduce both the number of needed tynodes in the stack, and the operational high voltage.

Acknowledgements

This work is supported by the ERC-Advanced Grant 2012 MEMBrane 320764.

Use of the National Synchrotron Light Source, Brookhaven National Laboratory, was supported by the US Department of Energy, Office of Science, Office of Basic Energy Sciences, under Contract no. DE-AC02-98CH10886. We are grateful to use the Low Energy branch of this radiation facility during the very last month of its existence. The photocathode work was supported by U.S. DoE, under KC0407-ALSJNT-I0013. We thank Johan Hidding (e-Science, the Netherlands) for the support of the low-energy Monte Carlo simulations in the form of a Pathfinder Grant.

We would like to thank FEI for making their low-energy extensions for GEANT-4 available for us. We thank Arjen van Rijn (Nikhef) for his energetic management of the MEMBrane project. We are grateful to Silvia Vangelista of Laboratorio MDM, IMM-CNR, for providing to us a MgO wafer. We thank Oscar van Petten (Nikhef) for the construction of the Dual Faraday Cup, and Berend Munneke (Nikhef) and Jan de Looff (ImPhys/TUD) for solving vacuum problems.

References

[1] M. Campbell, et al., Timepix, a 65 k programmable pixel readout chip for arrival time, energy and/or photon counting measurements, Nucl. Instrum. Methods Phys. Res. A 581 (2007) 485–494. http://dx.doi.org/10.1016/j.nima.2007.08.079.
[2] H. van der Graaf, et al., The readout of a GEM or Micromegas-equipped TPC by means of the Medipix2 CMOS sensor as direct anode, Nucl. Instrum. Methods A 535 (2004) 506–510.
[3] J. Vallerga, et al., Optical MCP image tube with a quad Timepix readout: initial performance characterisation, J. Instrum. 9 (2014) C05055. http://dx.doi.org/10.1088/1748-0221/9/05/C05055.
[4] H.van der Graaf, Signal Development and Processing in MWPCs (Ph.D. thesis), Delft University of Technology June, 1986.
[5] Y. Bilevych, S.E. Brunner, H.W. Chan, E. Charbon, H. van der Graaf, C.W. Hagen, G. Nützel, S.D. Pinto, V. Prodanović, D. Rotman, F. Santagata, L. Sarro, D.R. Schaart, J. Sinsheimer, J. Smedley, S.X. Tao, A.M.M.G. Theulings, Potential applications of electron emission membranes in medicine, Nucl. Instrum. Methods Phys. Res. 809 (2016) 171. http://dx.doi.org/10.1016/j.nima.2015.10.084.
[6] E.J. Sternglass, High-speed electron multiplication by transmission secondary electron emission, Rev. Sci. Instrum. 26 (12) (1955) 1202. http://dx.doi.org/10.1063/1.1715223.
[7] J. Cazaux, E-Induced secondary electron emission yield of insulators and charging effects, Nucl. Instrum. Methods Phys. Res. Sect. B: Beam Interact. Mater. At. 244 (2) (2006) 307–322. http://dx.doi.org/10.1016/j.nimb.2005.10.006.
[8] E.J. Sternglass, M.M. Wachtel, Transmission Secondary Electron Multiplication for High-Speed Pulse Counting, IRE Transactions on Nuclear Science, 1956, pp. 29–32.
[9] J. Barnard, I. Bojko, N. Hilleret, Measurements of the Secondary Electron Emission of Some Insulators, CERN-LHC Division.
[10] É.I. Rau, E.N. Evstaf'eva, M.V. Andrianov, Mechanisms of charging of insulators under irradiation with medium-energy electron beams, Phys. Solid State 50 (4) (2008) 621–630. http://dx.doi.org/10.1134/S1063783408040057.
[11] M. Bai, F. Pease, Electron beam induced conductivity in polymethyl methacrylate, polyimide, and SiO_2 thin films, J. Vac. Sci. Technol. B: Microelectron. Nanometer Struct. 22 (6) (2004) 2907. http://dx.doi.org/10.1116/1.1826062.
[12] W.E. Spicer, Photoemissive, photoconductive, and optical absorption studies of alkali-antimony compounds, Phys. Rev. 112 (1958) 114.
[13] J.J. Sheer, J. van Laar, GaAs-Cs: a new type of photoemitter, Solid State Commun. 3 (1965) 189.
[14] F.J. Himpsel, J.A. Knapp, J.A. van Vechten, D.E. Eastman, Quantum photoyield of diamond(111)-a stable negative-affinity emitter, Phys. Rev. B 20 (1979) 624.
[15] Raquel Maria Amaro Vaz, Studies of the Secondary Electron Emission from Diamond Films (Ph.D. thesis), Faculty of Science, School of Chemistry, University of Bristol, 2012.
[16] X.Y. Chang, Q. Wu, I. Ben-Zvi, A. Burrill, J. Kewisch, T. Rao, J. Smedley, E. Wang, E.M. Muller, R. Busby, D. Dimitrov, Electron beam emission from a diamond-amplifier cathode, Phys. Res. Lab. 105 (2010) 164801.
[17] S.X. Tao, A. Theulings, J. Smedley, H. van der Graaf, DFT study of electron affinity of hydrogen terminated β-Si_3N_4, Diam. Relat. Mater. 53 (2015) 52.
[18] S.X. Tao, A. Theulings, J. Smedley, H. van der Graaf, DFT study of electron affinity of alkali metal termination on clean and oxygenated β-Si_3N_4, Diam. Relat. Mater. 58 (2015) 214.
[19] G. Kresse, J. Furthmüller, Efficient iterative schemes for ab initio total-energy calculations using a plane-wave basis set, Phys. Rev. B 54 (1996) 11169.
[20] G. Kresse, J. Furthmüller, Efficient iterative schemes for ab initio total-energy calculations using a plane-wave basis set, J. Comput. Mater. Sci. 6 (1996) 15.
[21] S. Agostinelli, J. Allison, K. Amako, J. Apostolakis, H. Araujo, P. Arce, et al., GEANT-4 – a simulation toolkit, Nucl. Instrum. Methods Phys. Res. Sect. A: Accel. Spectrometers Detect. Assoc. Equip. 506 (2003) 250–303.
[22] E. Kieft, E. Bosch, Refinement of Monte Carlo simulations of electron–specimen interaction in low-voltage SEM, J. Phys. D: Appl. Phys. 41 (2008) 215310.
[23] Z. Czyżewski, D.O.N. MacCallum, A. Romig, D.C. Joy, Calculations of Mott scattering cross section, J. Appl. Phys. 68 (1990) 3066.
[24] H.J. Fitting, E. Schreiber, J.C. Kuhr, A. von Czarnowski, Attenuation and escape depths of low-energy electron emission, J. Electron Spectrosc. Relat. Phenom. 119 (2001) 35–47.
[25] E. Schreiber, H.J. Fitting, Monte Carlo simulation of secondary electron emission from the insulator SiO2, J. Electron Spectrosc. Relat. Phenom. 124 (2002) 25–37.
[26] R. Shimizu, D. Ze-Jun, Monte Carlo modelling of electron-solid interactions, Rep. Prog. Phys. 55 (1992) 487–531.
[27] B. Raftari, N.V. Budko, C. Vuik, Self-consistent drift-diffusion-reaction model for the electron beam interaction with dielectric samples, J. Appl. Phys. 118 (2015) 204101.
[28] H.-J. Fitting, M. Touzin, Time-dependant start-up and decay of secondary electron emission in dielectrics, J. Appl. Phys. 108 (2010) 033711.
[29] P.J. French, P.M. Sarro, R. Mallee, E.J.M. Fakkeldij, R.F. Wolffenbuttel, Optimization of a low-stress silicon nitride process for surface-micromachining applications, Sens. Actuators A 58 (1997) 149–157.
[30] B. Morana, G. Pandraud, J. Creemer, P.M. Sarro, Characterization of lpcvd amorphous SiC (a-SiC) as material for electron transparent windows, Mater. Chem. Phys. 139 (2013) 654–662.

[31] Steven M. George, Atomic layer deposition: an overview, Chem. Rev. 110 (1) (2010) 111–131.
[32] M.D. Groner, F.H. Fabreguette, J.W. Elam, S.M. George, Low-temperature Al_2O_3 atomic layer deposition, Chem. Mater. 16 (4) (2004) 639–645.
[33] Slade J. Jokela†, Igor V. Veryovkin†, Alexander V. Zinovev†, Jeffrey W. Elam††, Qing Peng††, Anil U. Mane††, The characterization of secondary electron emitters for use in large area photo-detectors, Appl. Accel. Res. Ind. AIP Conf. Proc. 1336 (2011) 208–212. http://dx.doi.org/10.1063/1.3586090.
[34] S.J. Jokela, I.V. Veryovkin, A.V. Zinovev, J.W. Elam, A.U. Mane, Q. Peng, Z. Insepov, Secondary electron yield of emissive materials for large-area micro-channel plate detectors: surface composition and film thickness dependencies, Phys. Procedia 37 (2012) 740–747. http://dx.doi.org/10.1016/j.phpro.2012.03.718.
[35] R.H. Fowler, Phys. Rev. 38 (1931) 45.
[36] M. Cardona, L. Ley (Eds.), Photoemission in Solids, Springer, Berlin, Germany, 1978.
[37] J. Hölzl, F.K. Schulte, Work functions of metals, in: G. Höhler (Ed.)Solid Surface Physics, Springer-Verlag, Berlin, 1979, pp. 1–150 http://dx.doi.org/10.1007/BFb0048919.
[38] J.J. Fijol, A.M. Then, G.W. Tasker, R.J. Soave, Secondary electron yield of SiO_2 and Si_3N_4 thin films for continuous dynode electron multipliers, Appl. Surf. Sci. 48–49 (C) (1991) 464–471. http://dx.doi.org/10.1016/0169-4332(91)90376-U.
[39] Suharyanto, Y. Yamano, S. Kobayashi, S. Michizono, Y. Saito, Secondary electron emission and surface charging evaluation of alumina ceramics and sapphire, IEEE Trans. Dielectr. Electr. Insul., 2006, 13(1), pp. 72–77. ⟨http://doi.org/10.1109/TDEI.2006.1593403⟩.
[40] J.B. Johnson, K.G. McKay, Secondary electron emission of crystalline MgO, Phys. Rev. 91 (3) (1953) 582–587. http://dx.doi.org/10.1103/PhysRev.91.582.
[41] A. Shih, J. Yater, P. Pehrsson, J. Butler, C. Hor, R. Abrams, Secondary electron emission from diamond surfaces, J. Appl. Phys. 82 (1997) (1997) 1860. http://dx.doi.org/10.1063/1.365990.
[42] Ramon U. Martinelli, M.L. Schultz, H.F. Gossenberger, Reflection and transmission secondary emission from GaAs, J. Appl. Phys. 43 (1972) 4803. http://dx.doi.org/10.1063/1.1661015.
[43] H. Qin, R. Tan, J. Park, H.S. Kim, R.H. Blick, Direct observation of sub-threshold field emission from silicon nanomembranes, J. Appl. Phys. 109 (12) (2011). http://dx.doi.org/10.1063/1.3597782.
[44] H. Jacobs, J. Freely, F.A. Brand, The mechanism of field dependent secondary emission, Phys. Rev. 88 (3) (1952) 492–499 (Retrieved from http://link.aps.org/doi/10.1103/PhysRev.88.492)..
[45] J.N. Heo, J.H. Lee, T.W. Jeong, C.S. Lee, W.S. Kim, Y.W. Jin, J.B. Yoo, Electron emission from carbon nanotube-dispersed MgO layer, Appl. Phys. Lett. 87 (11) (2005) 3–6. http://dx.doi.org/10.1063/1.2048814.
[46] The Large Area Picosecond Photon Detector project (LAPPD): ⟨http://psec.uchicago.edu⟩.
[47] Photonis: The Planacon Single Soft Photon Detector.
[48] Luca Cultrera, Hyeri Lee, Ivan Bazarov, J. Vac. Sci. Technol. B 34 (2016) 011202.
[49] Md Abdullah A. Mamun, Abdelmageed A. Elmustafa, Carlos Hernandez-Garcia, Russell Mammei, Matthew Poelker, J. Vac. Sci. Technol. A 34 (2016) 021509.
[50] S. Schubert, M. Ruiz-Oses, I. Ben-Zvi, T. Kamps, X. Liang, E. Muller, K. MÃ¼ller, H. Padmore, T. Rao, X. Tong, T. Vecchione, J. Smedley, APL Mater. 1 (2013) 032119.
[51] J.Smedley, et al., Sputter Growth of Alkali Antimonide Photocathodes: An In Operando Materials Analysis, Proceedings of IPAC2015, Richmond, VA, USA, 1965, 2015.⟨http://accelconf.web.cern.ch/AccelConf/IPAC2015/papers/tupha003.pdf⟩.
[52] G.F. Dionne, Origin of secondary-electron-emission yield-curve parameters, J. Appl. Phys. 46 (8) (1975) 3347–3351. http://dx.doi.org/10.1063/1.322061.